Ultrasonic Attenuation in Normal and Superconducting Indium*

E. S. Bliss† and J. A. Rayne
Carnegie-Mellon University, Pittsburgh, Pennsylvania 15213
(Received 24 July 1968)

Measurements of the electronic contribution to the attenuation of longitudinal sound waves propagating in normal and superconducting indium have been made up to 330 MHz. Data have been obtained for propagation along the principal crystallographic axes as well as for a number of directions in the (010) plane. The results exhibit considerable deviation from free-electron behavior. The limiting slopes of the attenuation versus frequency are highly anisotropic, and for quasi-longitudinal modes include a significant contribution which vanishes within approximately 30 mdeg of T_c. This drop is in addition to the less sudden drop associated with the BCS attenuation for longitudinal waves. Comparison of the measurements with simple calculations based on a modified free-electron model suggests that the effect of the crystal potential on the Fermi-surface topology is largely responsible for the observed attenuation behavior.

I. INTRODUCTION

In pure metals, the conduction electrons interact strongly with ultrasonic waves at low temperatures. The attenuation of an acoustic wave with phonon wave number q has been shown[1] to depend on the topology of the Fermi surface, its deformation properties under static strains, and the electron mean free path l. In the limit $ql \gg 1$, however, the dependence on l is negligible, and only electrons on the effective zone (those with velocity nearly perpendicular to the propagation direction) can contribute to the attenuation. Since the attenuation coefficient α approaches a linear dependence on the frequency f in this limit, determination of the limiting slope value $d\alpha/df$ in a particular propagation direction can provide information about the Fermi surface and its deformation properties on the associated effective zone.

Indium is well suited for such an investigation since its Fermi surface has approximately the free electron form,[2,3] and because the separation of electronic attenuation from other contributions is greatly simplified in superconductors.[4] It is also readily available in high purity form, and large single crystal ingots can be grown with relative ease, owing to its low melting point.

Previously reported measurements of attenuation in indium[5–9] show marked deviations from the free-electron predictions, considerable anisotropy in limiting slope values, and a significant amount of disagreement between the various sets of data. Although a wide variety of explanations has been offered for these effects, the discussion has remained essentially qualitative and the relative merit of the various explanations undetermined. This paper presents additional measurements and reports the results of numerical evaluation of the attenuation integrals for a simple modification of the free-electron Fermi surface. A detailed comparison of the data and calculations allows some conclusions to be drawn about the non-free-electron behavior of the attenuation.

II. EXPERIMENT

A. Experimental Procedure

The indium single crystals used in this work ranged in purity from 99.9% to 99.9999+%, and had residual resistance ratios measured by the eddy current technique[10] of approximately 200 to greater than 200 000. These crystals were grown in vacuum by a modified Bridgman technique from starting material supplied by Cominco American Incorporated of Spokane, Washington, and American Smelting and Refining Company of South Plainfield, New Jersey. The lowest purity material was obtained by suitable doping with lead. Acoustic specimens with faces normal to the required propagation directions were prepared from the single crystal ingots by spark erosion, with particular care being taken to minimize surface damage and consequent recrystallization. The extent of such surface damage was investigated by use of preferential etching and x-ray techniques and is believed to be limited to a depth of approximately 0.1 mm, about 3% of the smallest sample thickness. The final orientation of the samples was determined to within 1° by Laue back-reflection photographs.

Measurements of the relative attenuation of longitudinal and quasi-longitudinal waves in these samples were made in transmission using a pulse comparison

* Work supported by the National Science Foundation. This paper is based on a thesis submitted by one of us (E.S.B.) as partial fulfillment of the requirements for the Ph.D. degree in Physics at Carnegie-Mellon University.

† Present address: AFCRL, Hanscom Field, Bedford, Mass. 01730.

[1] A. B. Pippard, Proc. Roy. Soc. **A257**, 165 (1960).

[2] J. A. Rayne, Phys. Rev. **129**, 652 (1963).

[3] V. F. Gantmakher and I. P. Krylov, Zh. Eksperim. i Teor. Fiz. **49**, 1054 (1965) [English transl.: Soviet Phys.—JETP **22**, 734 (1966)].

[4] R. W. Morse and H. V. Bohm, Phys. Rev. **108**, 1094 (1957).

[5] K. Fossheim and J. R. Leibowitz, Phys. Letters **22**, 140 (1966).

[6] E. S. Bliss and J. A. Rayne, Phys. Letters **23**, 38 (1966); **23**, 560 (1966).

[7] V. D. Fil', O. A. Shevchenko, and P. A. Bezuglyi, Zh. Eksperim. i Teor. Fiz. **52**, 891 (1967) [English transl.: Soviet Phys.—JETP **25**, 587 (1967)].

[8] E. S. Bliss and J. A. Rayne, Phys. Letters **25A**, 242 (1967).

[9] A. C. E. Sinclair, Proc. Phys. Soc. **92**, 962 (1967).

[10] C. P. Bean, R. W. DeBlois, and L. B. Nesbitt, J. Appl. Phys. **30**, 1976 (1959).

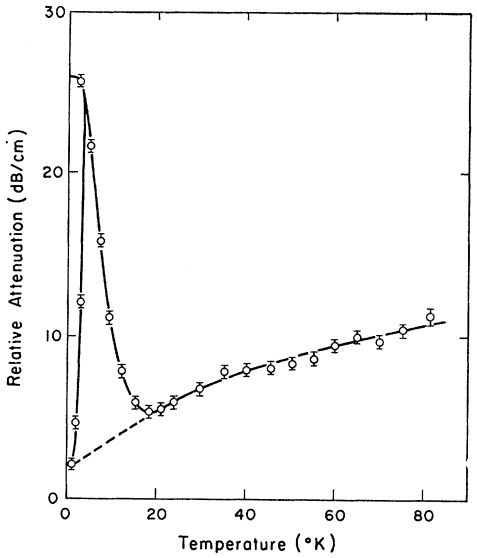

FIG. 1. Typical temperature dependence of the zero-amplitude attenuation for superconducting and normal indium up to 80°K. The dashed curve is the extrapolated behavior of the background attenuation due to nonelectronic interactions. The data were obtained at 90 MHz on 99.999% pure indium for (111) propagation.

technique. Data were obtained at frequencies as high as 330 MHz for propagation normal to the (100), (001), (110), (011), and (111) planes, as well as for a number of intermediate directions in the (010) plane. The acoustic waves were generated and received by 5, 10, and 30 MHz, x-cut quartz transducers, which operated at an odd harmonic and were bonded to the specimen faces by glycerin. A range of 70 dB in the amplitude of the input pulse could be produced by a calibrated attenuator at the transmitter output. The sample temeperature was automatically regulated by a feedback control system referenced to a carbon resistance thermometer between 1.1 and 30°K and a copper wire thermometer from 30°K to room temperature. Temperature measurements were made with a calibrated germanium thermometer (Honeywell MHSP 2404) below 100°K and a copper wire thermometer above that point. A longitudinal magnetic field of up to 700 G could be applied for making normal-state measurements below T_c. Measurements were subject to the following uncertainties: relative attenuation and applied amplitude to ± 0.2 dB, frequency to within 2%, temperature to ± 0.01°K at the lowest temperatures and ± 0.1°K above about 10°K, and magnetic field to within 3%.

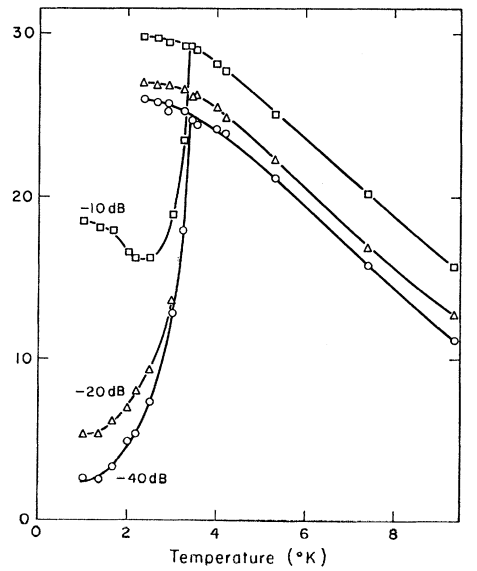

FIG. 2. Typical temperature and amplitude dependence of the superconducting and normal-state attenuation for indium between 1 and 10°K. The data were obtained at 90 MHz on 99.99% pure indium for (111) propagation.

B. Experimental Results

The quantity of initial interest is the electronic contribution α_{ne} to the normal-state attenuation α_n at low temperatures. In the present case, measurement of this parameter is simplified since it is known[4,11] that the electronic part α_{se} of the superconducting attenuation α_s goes to zero as the temperature approaches 0°K. Thus if α_n and α_s are both extrapolated to 0°K, their difference at that point should be α_{ne}. This is illustrated in Fig. 1, which demonstrates that an extrapolation of the background (nonelectronic) attenuation to 0°K agrees with the zero-temperature value of α_s. Further the temperature-dependent ratio α_{se}/α_{ne} can be compared with the BCS theory[4,11] to obtain a measure of the superconducting energy gap.

The attenuation of indium in both the normal and superconducting states exhibits a dependence on transmitter pulse amplitude[6,12,13] similar to that found in lead.[14–16] Figure 2 shows typical behavior for the temperature and amplitude dependence of α_n and α_s between 1 and 10°K. Since the effect of amplitude is different in the normal and superconducting states, except for the low-purity samples or at very low frequencies, both the difference $\alpha_n - \alpha_s$ and the apparent value of α_{se}/α_{ne} are also functions of amplitude. To correct for this dependence, data were taken over a range of amplitudes at each temperature and extrapolated to zero amplitude. This procedure is truly satisfactory only when data can be taken at low enough amplitudes that the attenuation-versus-amplitude curve

[11] J. Bardeen, L. N. Cooper, and J. R. Schrieffer, Phys. Rev. **108**, 1175 (1957).
[12] P. A. Bezuglyi, V. D. Fil', and O. A. Shevchenko, Zh. Eksperim. i Teor. Fiz. **49**, 1715 (1965) [English transl.: Soviet Phys.—JETP **22**, 1172 (1966)].
[13] E. S. Bliss and J. A. Rayne, Bull. Am. Phys. Soc. **11**, 241 (1966).
[14] R. E. Love and R. W. Shaw, Rev. Mod. Phys. **136**, 260 (1964).
[15] B. R. Tittmann and H. E. Bömmel, Phys. Rev. Letters **14**, 296 (1965).
[16] B. R. Tittmann and H. E. Bömmel, Phys. Rev. **151**, 178 (1966).

begins to flatten out. In general, this is fairly easy to accomplish for low-purity samples, but it becomes more difficult as the purity increases. When this condition is not met, larger error estimates must be assigned to allow for inaccuracies in the extrapolation. The error from this source and from the magnetoacoustic effects to be discussed later often makes fitting to the BCS theory a rather insensitive method for determining the superconducting energy gap. This being the case, no energy-gap values are reported here.

It is claimed by some authors[9,17] that the same mechanism responsible for the amplitude effect, namely, dislocation damping, makes a significant contribution to α_n and α_s even at zero amplitude. For reasons to be discussed in Sec. III A, we assume that the effect of this contribution on $\alpha_n-\alpha_s$ is negligible.

Another problem in the measurements is the appearance of magnetoacoustic effects under application of even the rather weak magnetic field (283 G or less[18]) required to keep the metal in its normal state. These effects are most pronounced for very pure samples and are usually difficult to extrapolate to zero field. Figure 3(a) shows typical attenuation versus field data at five temperatures near and below T_c. To separate the effects of field and temperature dependence in the normal state, the magnetic field is increased in steps as the temperature is lowered below T_c. That is, at constant field, the temperature is lowered nearly to the point at which the superconducting transition would occur; then, at constant temperature, the field is increased by 50 to 75 G and the process repeated until the lowest temperature is reached. The data are then reduced by subtracting all attenuation changes which occur when the field is varied. This procedure appears to be the most reasonable correction method available and leads to no unexpected or inconsistent results. Nevertheless, as with the amplitude effect, uncertainties due to this procedure must be considered when assigning error estimates to the results. For some orientations, the attenuation-versus-field curves display the much more convenient form shown in Fig. 3(b). In this case, it is assumed that the zero field extrapolation can be obtained by extending the curve about which the attenuation oscillates.

Using these established procedures to compensate for such obvious complications, it has been possible to measure α_{ne} extrapolated to 0°K for a number of purities and propagation directions. A detailed study of the dependence of attenuation on the acoustic wave number q and the electronic mean free path l has been conducted for propagation normal to the (111) plane.[8] Figures 4 and 5 show, respectively, the frequency dependence of α_{ne} and the ratio of attenuation divided by frequency, α_{ne}/f, for samples of three, four, five, and six nines plus purity with this direction of propagation. It can be seen that at high frequencies and for the purest samples ($ql\gg1$) the attenuation is proportional to the frequency, whereas at low frequencies and for the less pure samples ($ql\ll1$) it varies quadratically with frequency. As discussed in Sec. III, this dependence is predicted by theoretical considerations,[19] which also show that for a given propagation direction α/f is a

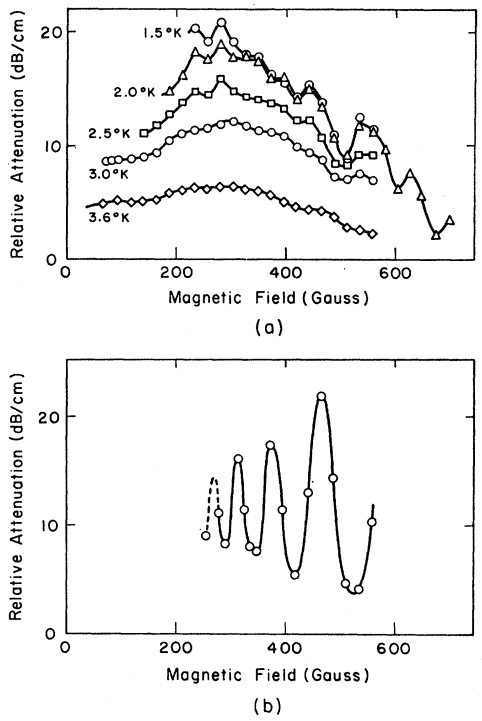

FIG. 3. (a) Typical variation of the attenuation with magnetic field due to the magnetoacoustic effect. The data were obtained at 90 MHz on 99.999+% pure indium with propagation 25° from [001] in the (010) plane. (b) More desirable variation of the attenuation with magnetic field. The data were obtained at 150 MHz on 99.9999+% pure indium with propagation 37° from [001] in the (010) plane.

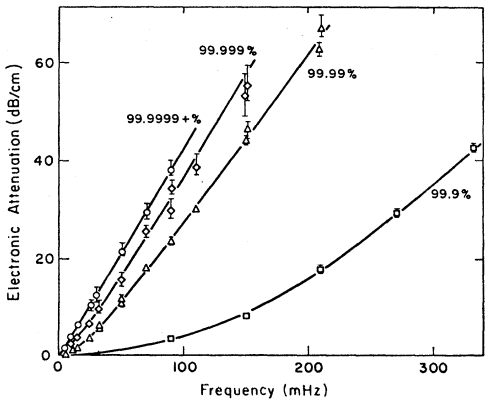

FIG. 4. Frequency dependence of the normal-state electronic attenuation for longitudinal waves in indium of varying purity. The propagation direction is along the normal to the (111) plane.

[17] W. P. Mason, Phys. Rev. 143, 299 (1966).
[18] D. K. Finnemore and D. E. Mapother, Phys. Rev. 140, A507 (1965).
[19] A. B. Pippard, Phil. Mag. 46, 1104 (1955).

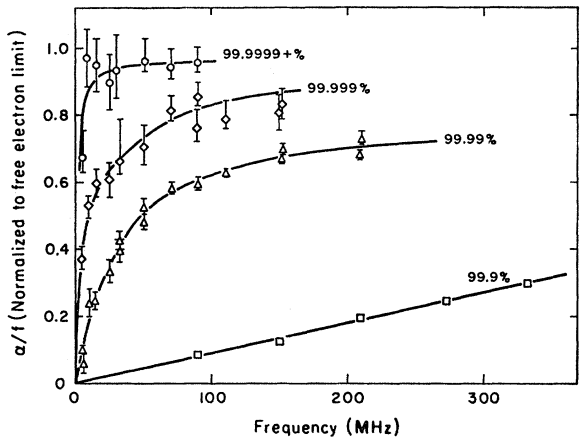

FIG. 5. Variation of α/f versus f for the normal-state electronic attenuation for longitudinal waves in indium of varying purity. The propagation direction is along the normal to the (111) plane.

function of the product ql. This conclusion can be tested by determining whether it is possible to scale the frequency values for each specimen purity, such that all the data for α_{ne}/f lie on a common smooth curve as ql varies from zero to its highest value. This procedure should be equivalent to multiplying the frequency in each case by the ratio $l/l_{\text{reference}}$. The scaling factors so determined agree, within experimental error, with mean free path ratios obtained from approximate residual resistance measurements. The results of this analysis are shown in Fig. 6.

For other propagation directions, measurements have been performed only on high purity 99.9999% and 99.9999+% samples to determine the limiting values of $d\alpha_{ne}/df$. All the curves of attenuation versus frequency are similar to those for the 99.9999+% sample in Fig. 4. The resulting slopes for propagation along axes of high symmetry are given in Table I, together with the data of other workers.[5,7,9] The agreement between the various experiments is rather poor. It is noteworthy, however, that in all cases the observed values of $d\alpha_{ne}/df$ for **q** parallel to [100] and [001] are much lower than for other propagation directions.

TABLE I. Measured values of the limiting slopes $d\alpha/df$ for longitudinal waves propagating along the principal crystallographic directions in pure indium. The data are compared with the results of other workers and also with the predictions of the free-electron model.

Propagation direction	Present work	$d\alpha/df$ (dB/cm MHz) B.[a]	S.[b]	F.L.[c]	F.E.[d]	$d\alpha/df$ normalized to free-electron value
[100]	0.234±0.010	0.158	0.260	0.217	0.497	0.47
[001]	0.270±0.010	0.185	0.266	0.236	0.519	0.52
[110]	0.397±0.015	0.330	0.392	0.356	0.429	0.93
(011)	0.430±0.015	0.339	···	···	0.471	0.91
(111)	$0.424^{+0.021}_{-0.012}$	0.301	0.318	···	0.440	0.96

[a] See Ref. 7. [b] See Ref. 9. [c] See Ref. 5.
[d] Computed for 3 electrons/atom and sound velocities extrapolated to absolute zero from Ref. 20.

The observed limiting slopes can be compared with the predictions of the free-electron model,[19] viz.,

$$\lim_{ql\to\infty}(d\alpha/df)=\tfrac{1}{3}\pi^2(N\hbar k_0/Mv_s^2), \qquad (1)$$

where N is the number density of conduction electrons, k_0 is the radius of the Fermi sphere, M is the density of the metal and v_s is the sound velocity appropriate to the propagation direction. Table I gives the calculated free-electron slopes for indium, assuming three conduction electrons per atom and using values of v_s obtained from the elastic constants extrapolated to absolute zero.[20] Also shown are the ratios of the latter to the values of $d\alpha_{ne}/df$ obtained in the present experiments. For [100] and [001] propagation it can be seen that the observed slope is only about one half the free-electron value, while for the other directions it is quite close to the free-electron limit.

The results for propagation of quasi-longitudinal waves in the (010) plane are shown in Table II and Fig. 7. It is clear that the limiting slopes are highly anisotropic, there being a particularly large limiting slope for **q** approximately 25° from [001]. In an attempt to determine the cause of this behavior, the temperature variation of the attenuation has been studied immediately below T_c.[21] The possible importance of such measurements is suggested by the recent observation[22] of an extremely rapid drop in the superconducting

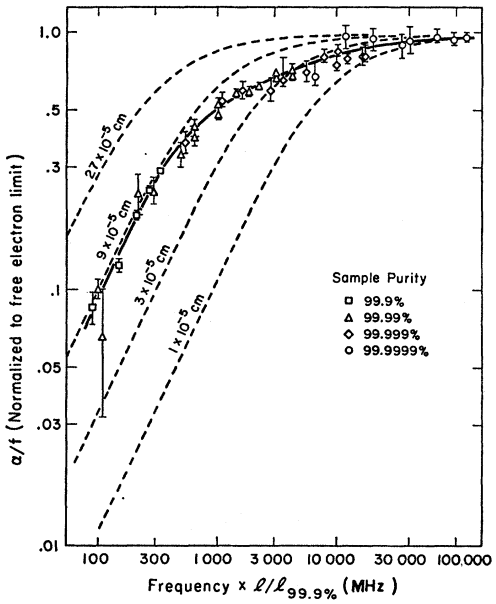

FIG. 6. Variation of α/f versus f for the normal-state electronic attenuation of longitudinal waves propagating along (111) in indium. The dashed curves are the predictions of the free-electron model for assumed values of $l_{99.9\%}$, the electronic mean free path corresponding to the sample of lowest purity.

[20] B. S. Chandrasekhar and J. A. Rayne, Phys. Rev. **124**, 1011 (1961).
[21] E. S. Bliss and J. A. Rayne, Phys. Letters **26A**, 278 (1968).
[22] J. M. Perz, Can. J. Phys. **44**, 1765 (1966).

attenuation of quasi-longitudinal waves in white tin very close to the critical temperature. Our data show that this effect is also present in indium for quasi-longitudinal modes, being especially large for some directions of propagation. In a few cases the decrease within 20 mdeg of T_c accounts for nearly 50% of the total normal-state electronic attenuation.

Figure 8 is an example of the kind of data obtained from these measurements. It also illustrates the fitting procedure used to extract that part of the temperature dependence of α_{se} which is predicted by the usual BCS expression. The initial plan was first to calculate the BCS attenuation, using the estimated point of intersection with the line $T=T_c$ and a reasonable value of the superconducting energy gap, and then to follow an iterative procedure with the intercept and energy gap being adjusted until the best fit to the data below about T_c -0.03°K was obtained. In practice, the comparison between theory and data is made by superimposing a graph of the BCS calculations over a graph of the data. It has been found that changing the intercept and the energy gap within the appropriate ranges has an effect essentially equivalent to raising or lowering and rotating the initial BCS graph with respect to the data. Thus the best curve through the data can be obtained by physically displacing and/or rotating the BCS graph based on an initial intercept estimate and an energy gap of 1.75 k_BT_c. The BCS calculations are made using an approximate analytic expression[23] for the temperature-dependent energy gap $\Delta(t)$ modified by an additional small correction term. The modified form,

$$\Delta(t)/\Delta(0)=(\cos\tfrac{1}{2}\pi t^2)^{1/2}-1.15\times10^{-3}e^{3.8t}\times\sin[5.46(1-t)], \quad (2)$$

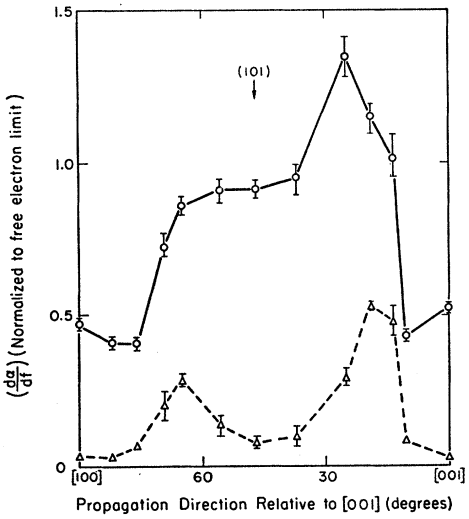

FIG. 7. Variation of the limiting slope $d\alpha/df$, normalized to the free-electron value, for quasi-longitudinal waves propagating in the (010) plane of indium. The dashed line is the component of $d\alpha/df$ associated with the rapid fall of the superconducting attenuation near T_c.

[23] T. P. Sheahen, Phys. Rev. **149**, 368 (1966).

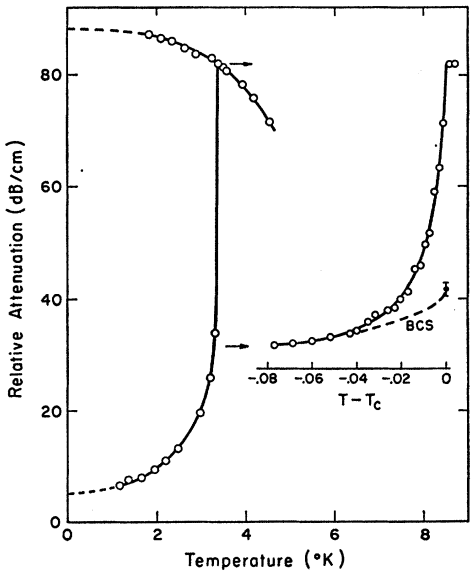

FIG. 8. Temperature dependence of the electronic attenuation near T_c for a 150 MHz quasi-longitudinal mode propagating in the (010) plane of 99.9999+% pure indium with q approximately 19° from [001]. The dashed line in the inset is the BCS prediction for $\Delta=1.75k_BT_c$.

gives a maximum departure from Mühlschlegel's tabulation[24] of less than 0.5% as compared with about 3.1% for Sheahen's cosine function alone. The part of the rapid fall, which remains after the BCS prediction is subtracted, is given by the bottom curve in Fig. 7. Such a plot emphasizes the anisotropy of the effect and the fact that it makes a considerable contribution to the total observed attenuation in some propagation directions. The rapid-fall contribution to $d\alpha/df$ is also given in Table II.

TABLE II. Measured values of the limiting slopes $d\alpha/df$ for quasi-longitudinal waves propagating in the (010) plane of pure indium. The contribution arising from the rapid drop in attenuation near the transition temperature is also given. In both cases the results are given in dB/cm MHz and normalized to the free-electron value.

Propagation direction (degrees from [001])	$(d\alpha/df)_{\text{total}}$ (dB/cm MHz)	$(d\alpha/df)_{\text{total}}$ Normalized to free-electron value	$(d\alpha/df)_{\text{rapid drop}}$ (dB/cm MHz)	$(d\alpha/df)_{\text{rapid drop}}$ Normalized to free-electron value
[001]	0.270 ± 0.010	0.521 ± 0.019	0.015 ± 0.005	0.028 ± 0.009
10.5	$0.220^{+0.011}_{-0.007}$	$0.430^{+0.021}_{-0.014}$	0.043 ± 0.005	0.083 ± 0.009
13.5	$0.515^{+0.039}_{-0.031}$	$1.012^{+0.077}_{-0.061}$	0.245 ± 0.024	0.482 ± 0.047
19.0	$0.575^{+0.019}_{-0.028}$	$1.148^{+0.038}_{-0.056}$	0.267 ± 0.008	0.532 ± 0.015
25.0	0.662 ± 0.035	1.351 ± 0.071	0.145 ± 0.015	0.295 ± 0.030
37.1	$0.452^{+0.020}_{-0.030}$	$0.952^{+0.042}_{-0.063}$	0.047 ± 0.017	0.099 ± 0.036
(101)	0.430 ± 0.015	0.913 ± 0.032	0.036 ± 0.011	0.075 ± 0.022
55.6	0.431 ± 0.020	0.911 ± 0.042	0.066 ± 0.017	0.139 ± 0.036
65.0	0.412 ± 0.015	0.859 ± 0.031	0.138 ± 0.011	0.286 ± 0.022
69.2	$0.350^{+0.025}_{-0.018}$	$0.723^{+0.052}_{-0.031}$	0.100 ± 0.026	0.206 ± 0.054
76.2	0.199 ± 0.010	0.406 ± 0.020	0.033 ± 0.006	0.066 ± 0.011
82.0	0.203 ± 0.010	0.410 ± 0.020	0.015 ± 0.007	0.029 ± 0.013
[100]	0.234 ± 0.010	0.471 ± 0.020	0.017 ± 0.005	0.034 ± 0.010

[24] B. Mühlschlegel, Z. Physik **155**, 313 (1959).

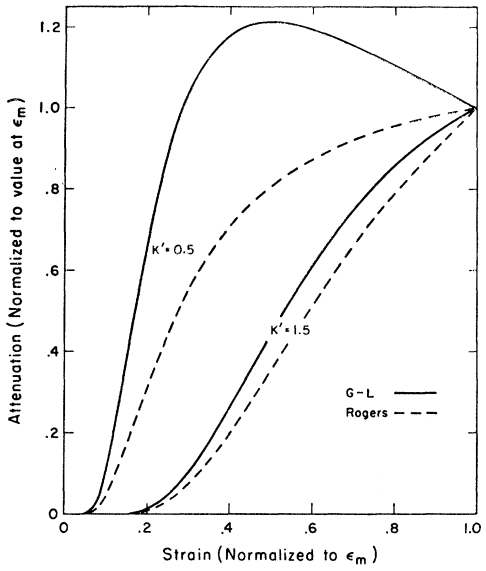

FIG. 9. Theoretical dependence on strain amplitude of the breakaway dislocation attenuation α_b given by Eqs. (3) and (4), and the dynamical attenuation α_{dR} given by Eqs. (6) and (7). The curves are all normalized to the value of attenuation at the maximum strain amplitude ϵ_m.

III. THEORY

A. Dislocation Attenuation

An amplitude dependence of the type shown in Fig. 2 is thought to be caused by dislocation attenuation.[15–17,25] Granato and Lücke,[26] hereafter referred to as G-L, have calculated the properties of a model in which damped dislocation loops break away from intermediate pinning points. Their expression for amplitude dependent attenuation due to the breakaway mechanism is

$$\alpha_b=\alpha_{b0}(K/\epsilon_0)\exp(-K/\epsilon_0). \quad (3)$$

In this equation ϵ_0 is the longitudinal strain amplitude, while α_{b0} and K are parameters which depend on the properties of the dislocation network.

Because only relative transmitter amplitude and relative attenuation are known in our experiments and because reliable values are unavailable for many of the other quantities in Eq. (3), the ways in which measured attenuation versus amplitude curves can be compared with the theory are limited. One possibility is to normalize α_b in Eq. (3) to its value α_{bm} at some maximum strain amplitude ϵ_m. If K' is substituted for K/ϵ_m, then Eq. (3) gives

$$\alpha_b/\alpha_{bm}=(\epsilon_m/\epsilon_0)\exp[K'(1-\epsilon_m/\epsilon_0)]. \quad (4)$$

Thus a variation in the value of K' generates a family of curves which can be compared to data normalized in the same way. Figure 9 shows Eq. (4) plotted for two K' values, while Fig. 10 shows typical data for the lowest temperature normalized to three different ϵ_m values. As can be seen from the latter figure, it is possible to get a rough fit to the low amplitude data by choosing a large value of K', but the agreement is still disappointing and is especially bad for the higher amplitudes. A more frequently used method of comparison[16,27] is illustrated in Fig. 11, where the lowest temperature data is plotted in the form $\ln(\alpha_b\epsilon_0)$ versus $1/\epsilon_0$. According to Eq. (3) such a plot should give a straight line with slope $-K$ and intercept $\ln(\alpha_{b0}K)$. Clearly this prediction is not realized.

The discrepancies between this work and the G-L expression can probably be traced to one or more of the simplifying assumptions made in its derivation. These assumptions restrict the validity of Eq. (3) to frequencies much less than the resonant frequency of the dislocation loops, to amplitudes sufficient to unpin only a small fraction of the dislocations ($K'\gg1$), and to rather impure material in which L_N, the separation of network pinning points, is large compared to L_C, the separation of point defect pinning points. Since all of these restrictions are probably violated in our measurements, it is not surprising that the quantitative agreement is poor. Nevertheless, all of the qualitative predictions of the model that can be checked are verified experimentally. For example, the decrease in electron damping in the superconducting state should result in an enhanced dependence on amplitude as the temperature is lowered below T_c. Such an enhancement is evident in Fig. 2, which also shows the damping to be essentially temperature-independent in the normal state.

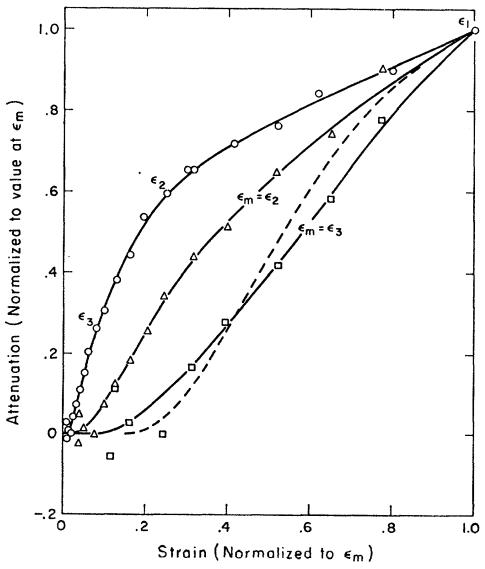

FIG. 10. Typical experimental data for the strain amplitude dependence of the attenuation in the superconducting state of indium normalized to three different maximum strain values. The dashed curve is the Granato-Lücke prediction for K' equal to 1.5.

[25] B. R. Tittmann and H. E. Bömmel, Bull. Am. Phys. Soc. **9**, 713 (1964).

[26] A. Granato and K. Lücke, J. Appl. Phys. **27**, 583 (1956).

[27] A. Granato and K. Lücke, J. Appl. Phys. **27**, 789 (1956).

A further conclusion can be drawn from the more generally valid G-L expression for loop displacement. This expression is a sum over i of terms containing $[(\omega_{iL}^2-\omega^2)^2+(\omega B/A)^2]^{1/2}$ in the denominator, where $\omega_{iL}=(2i+1)(\pi/L)(C/A)^{1/2}$, L is the loop length, A is the effective loop mass per unit length, and B is the damping coefficient in the equation of motion for a dislocation loop. It can be seen that for either low frequencies or small L the importance of the term containing B is diminished, and the amplitude dependence of α_s and α_n should be more nearly the same. This prediction is confirmed by experiment. An increase of the frequency such that $(\omega_{iL}^2-\omega^2)^2\gg(\omega B/A)^2$ should have a similar effect. When $\omega=\omega_{iL}$ the other extreme occurs, i.e., B becomes very important and α_n and α_s should show markedly different dependence on amplitude. It might, in fact, be possible to determine ω_{0L} by making a detailed study of the relative effect of strain amplitude on α_n and α_s as a function of frequency. Such a determination has not been attempted in this work.

Since Eq. (3) depends on the assumption that dislocation loops vibrate in phase with the applied stress, it describes a static type of loss with frequency entering only in the proportionality between α and $\Delta W/W$. However, there is also a dynamic loss, since the dislocation motion is opposed by damping, and hence must actually lag behind the oscillating stress by a frequency-dependent phase angle. The G-L expression for attenuation due to this mechanism can be written

$$\alpha_{dL}=C_1C_L\Lambda\{(\omega_{0L}A)^2B/[(\omega_{0L}A)^2(\Omega_L^{-1}-\Omega_L)^2+B^2]\}, \quad (5)$$

where $\Omega_L=\omega/\omega_{0L}$ and $C_L=\pi L^2/A$. Both C_1 and Λ are constants depending on the properties of the metal and the dislocation network. The effect of a distribution of loop lengths can be approximated by substituting for L an effective value L_{eff} larger than L_{ave}.

A generalization of the G-L derivation for breakaway attenuation, valid to higher amplitudes and for smaller values of L_N/L_C, has been given by Rogers.[28] However, the resulting expression for α_b does not display any new qualitative features and is still limited to frequencies much less than ω_{0L}. The dynamic loss is also discussed and shown to exhibit an amplitude dependence of its own due to increased attenuation by the longer unpinned loops. This dependence is given, for all frequencies and amplitudes, by

$$\alpha_{dR}=\alpha_{dL_N}\{1-[1-(K/\epsilon_0+1)\exp(-K/\epsilon_0)]^n\}+\alpha_{dL_C}\{\text{term decreasing from 1 to 0 with increasing } \epsilon_0\}, \quad (6)$$

where α_{dL_N} is the dynamic attenuation of Eq. (5) with $L=L_N$ and $n=L_N/L_C-1$. Since for all n the term multiplying α_{dL_N} simply varies from 0 to 1 as ϵ_0 is increased, the main interest is in the factor α_{dL_N}. The ratio $\alpha_{dL_N}/\alpha_{dL_C}$ is equal to $(L_N/L_C)^4$ for $1\gg\Omega_{L_C}\ll\omega_{0L_C}A/B$, and approximately equal to unity for $\Omega_{L_C}>1$, as can be seen by considering the L dependence of C_L, ω_{0L}, and Ω_L in Eq. (5). By normalizing the L_N part of α_{dR} in the same way as α_b, their variation with amplitude can be compared:

$$\alpha_{dR}/\alpha_{dR_m}\simeq\frac{(1+K'\epsilon_m/\epsilon_0)}{(1+K')}\exp K'(1-\epsilon_m/\epsilon_0). \quad (7)$$

Equation (7) is plotted for two values of K' in Fig. 9. It is seen that α_b and α_{dR} exhibit identical dependence on amplitude for large K', but that for K' on the order of unity or less α_b passes through a maximum while α_{dR} does not. Clearly it is desirable to establish whether one or the other of these contributions is dominant. Rogers plots two sets of curves showing combined dynamic and breakaway loss versus amplitude, assuming $\alpha_{b0}/\alpha_{dL_N}=n$ and $10n$, respectively. These curves seem to compare favorably with recent measurements in lead.[29]

We now consider the predictions of these expressions with respect to the magnitude of zero amplitude dislocation attenuation. Equation (5) indicates that, even for the limit of zero applied stress, there is an attenuation which depends on the damping coefficient B. Since B is always smaller in the superconducting state, the contributions to α_s and α_n differ, and $\alpha_n-\alpha_s$ does not give a true measure of the electronic attenuation. Attempts have been made[16] to minimize the importance of this dynamic loss by pointing out that it is not valid to calculate B due to electrons by use of electron-viscosity concepts, unless the product of a typical Fourier component of the dislocation strain field and the electron mean free path l is much less than unity, a

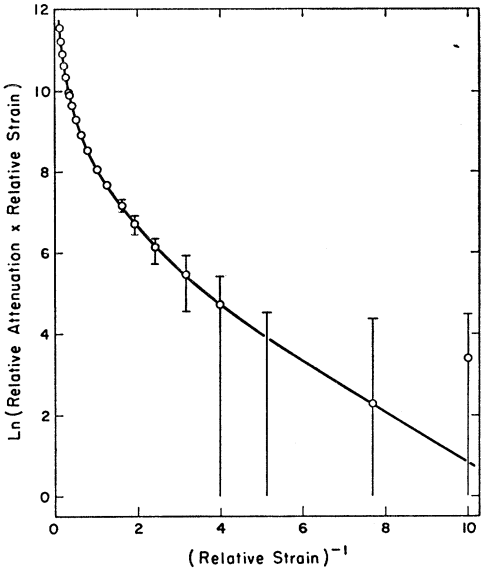

FIG. 11. Typical Granato-Lücke plot of the measured strain-amplitude-dependent attenuation in indium.

[28] D. H. Rogers, J. Appl. Phys. 33, 781 (1962).

[29] A. Hikata and C. Elbaum, Phys. Rev. Letters 18, 750 (1967).

requirement not met in reasonably pure metals at low temperatures. While this statement is true, it does not invalidate the use of Eq. (5) with a properly calculated B.

The real question is not whether the dynamic loss is present, but whether it is small compared with the electronic attenuation. From the discussion following Eq. (6), it can be said that the zero-amplitude dislocation attenuation α_{dL_C} will in no case exceed that part of the high-amplitude attenuation due to dynamic effects α_{dL_N} and that it may be much less. In addition, the comments following Eq. (7) indicate that α_{dL_N} is less than or equal to α_{b0}. As an example, consider the lead data[15-16] used in a recent paper[17] concerning the importance of α_{dL_C}. If $n=L_N/L_C-1\cong 10$, $\alpha_{dL_N}\cong\alpha_{b0}/10n$, $\alpha_{b0}\cong 10$ dB/cm, and $\Omega_{L_C}<1$ so that $\alpha_{dL_C}/\alpha_{dL_N}<1$, then $\alpha_{dL_C}<0.1$ dB/cm and the contribution to $\alpha_n-\alpha_s$ from zero-amplitude attenuation would be on the order of 1% or less. Even if a large correction should be made, however, it is not clear whether the correction term would increase or decrease with temperature, since Eq. (5) has a maximum as a function of B and the value of B at this maximum is a function of ω. Because the effect appears too small and its sign is uncertain, we have made no correction for zero-amplitude dislocation attenuation.

B. Electronic Attenuation

According to the theory of normal-state electronic attenuation in real metals, the expression for attenuation of an acoustic wave of arbitrary polarization and propagation direction is[1]

$$\alpha_{ne}=\frac{\hbar q}{4\pi^3 M v_s}\left\{\int\frac{\mathfrak{D}^2 a\,dS}{1+a^2\cos^2\phi}+B_{ij}I_iI_j\right\}, \tag{8}$$

where $a=ql$, and ϕ is the angle between the electron velocity $\mathbf{v}_e$ and the propagation direction of the acoustic wave, taken to be along the x coordinate axis. $\mathfrak{D}$ is given by $\mathbf{D}\cdot\mathbf{u}/u$, where $\mathbf{u}$ is the particle velocity and $\mathbf{D}(\mathbf{k})=\mathbf{K}(\mathbf{k})+\mathbf{k}\cos\phi$. In the latter expression $\mathbf{k}$ is the electron wave vector and $\mathbf{K}(\mathbf{k})$ the vector deformation coefficient, which is defined such that a strain $\mathbf{e}$ causes a shift of the Fermi surface by an amount $\mathbf{K}\cdot\mathbf{e}$ normal to itself. The coefficients B_{ij} are given by the relation $B_{ij}=(A^{-1})_{ij}$, where the A_{ij} are integrals over the Fermi surface:

$$A_{ij}=\int\frac{a_ia_j dS}{a(1+a^2\cos^2\phi)}. \tag{9}$$

The I_i are also surface integrals and are given by

$$I_i=\int a_i\left(\frac{\mathfrak{D}a\cos\phi}{1+a^2\cos^2\phi}\right)dS. \tag{10}$$

For the particular case of pure longitudinal waves, $\mathfrak{D}=K_x+k_x\cos\phi$ and the limiting forms of Eq. (8) are

$$\alpha_{a\ll 1}\cong\frac{\hbar q^2}{4\pi^3 M v_s}\int\mathfrak{D}^2 dS, \tag{11}$$

and

$$\alpha_{a\gg 1}\cong\frac{\hbar q}{4\pi^2 M v_s}\oint RK_x^2 d\psi, \tag{12}$$

where R is the reciprocal of the Gaussian curvature of the Fermi surface and ψ specifies the position of the projection of $\mathbf{v}_e$ in the y, z plane. The integral on ψ is taken around the effective zone defined by $\phi=\frac{1}{2}\pi$, indicating that in the high ql limit only those electrons with velocity approximately perpendicular to the direction of propagation can contribute. Equations (11) and (12) show the limiting quadratic and linear frequency dependence mentioned previously. In the free-electron approximation $K_x=-\frac{1}{3}k_0$, where k_0 is the radius of the Fermi sphere. Equation (11) then reduces to

$$\alpha_{\text{f.e.}}=\frac{N\hbar k_0}{Mlv_s}\left\{\frac{a^2\tan^{-1}a}{3(a-\tan^{-1}a)}-1\right\}. \tag{13}$$

Note that α/f exhibits a progressively weaker dependence on a until, as seen from Eq. (12), it reaches a limiting value independent of a.

For propagation directions in which the acoustic wave is not purely longitudinal, Eqs. (11) to (13) are not correct, but Eq. (8) can still be simplified somewhat for $a\gg 1$ by dropping terms which go to zero as $1/a$. If in addition $\mathbf{u}$ is chosen to be in the x, y plane and Ω is the angle between $\mathbf{q}$ (the x axis) and $\mathbf{u}$, then[22]

$$\alpha_{ne}=(\hbar q/4\pi^2 M v_s)(J_1+J_2), \tag{14}$$

where J_1 and J_2 are given by

$$J_1=\cos^2\Omega\oint RK_x^2 d\psi+2\sin\Omega\cos\Omega\oint RK_xK_y d\psi+\sin^2\Omega\oint RK_y^2 d\psi, \tag{15}$$

and

$$J_2=L_1\cos^2\Omega+L_2\sin\Omega\cos\Omega+L_3\sin^2\Omega. \tag{16}$$

Here L_1, L_2, and L_3 contain integrals over the whole Fermi surface.

In the superconducting state for $a\gg 1$, the general equation for superconducting electronic attenuation reduces to

$$\alpha_{se}=(\hbar q/4\pi^2 M v_s)J_1\times 2f(\Delta), \tag{17}$$

where $f(\Delta)$ is the Fermi function of the superconducting energy-gap parameter. From a comparison of Eqs. (14) and (17) it is clear that if $J_2=0$, which is true for pure longitudinal modes ($\Omega=L_1=0$), then the usual BCS expression[4,11] holds and $\alpha_{se}/\alpha_{ne}=2f(\Delta)$. Otherwise,

$$\alpha_{ne}=\alpha_{se}/2f(\Delta)+[\hbar q/4\pi^2 M v_s]J_2, \tag{18}$$

indicating a rapid drop at T_c equal to the term containing J_2, due to the loss of electromagnetic coupling in the superconducting state. This drop is in addition to the less sudden decrease of $f(\Delta)$ below T_c.

IV. DISCUSSION

A. Pure-Mode Attenuation

Ideally, the data should be compared with Eq. (8), allowing for the full range of ql values and for deviations from purely longitudinal polarization. However, evaluation of this equation requires a complete knowledge of the Fermi surface, including the deformation parameter and mean free path at all points on it. Since the Fermi surface of indium is only approximately known, especially with respect to the geometry of the third zone arms, and since we can only guess at the anisotropy of $\mathfrak{D}$ and l, the errors involved in using the appropriate simplified forms of the theory will be negligible.

In the free-electron pure-mode approximation given by Eq. (13), we can calculate curves of α/f versus ql for given values of l. Four such curves are plotted in Fig. 6 together with the data for propagation normal to the (111) plane, which is a nearly pure mode direction for longitudinal waves. At low frequencies, the data are fitted by the free-electron theory for a mean free path of 9×10^{-5} cm. This figure corresponds to a ql value of approximately 0.2 for the least pure sample at 90 MHz and agrees within a factor of 2 with surface-impedance estimates.[30] In this orientation at the high frequency extreme ($ql\cong200$), the data give a measured limiting value of $d\alpha/df$ which agrees with the free-electron value within experimental error (see Table I). For the intermediate ql range, however, the data show a definite departure from the free-electron theory. This result differs from that previously reported for polycrystalline indium,[31] suggesting some anisotropic effect not accounted for by the free-electron assumption. It is also clear that previous analyses of attenuation experiments,[9] involving the use of the free-electron theory to obtain information about the mean free path l, may give incorrect results.

From the temperature dependence of the attenuation of a given sample at *fixed* frequency, it is possible to obtain an analogous plot of α/f versus ql for phonon rather than impurity scattering. The resulting behavior for propagation normal to (111) is quite similar to that shown in Fig. 6, the curve being flatter than the free-electron prediction at intermediate values of ql. Because of the uncertain background (nonelectronic) attenuation at higher temperatures, however, it is found that there is considerable scatter in such plots even for the same sample at different frequencies. Thus there has been no attempt to infer any differences in the behavior of the attenuation in indium due to small-angle phonon scattering and large-angle impurity scattering.

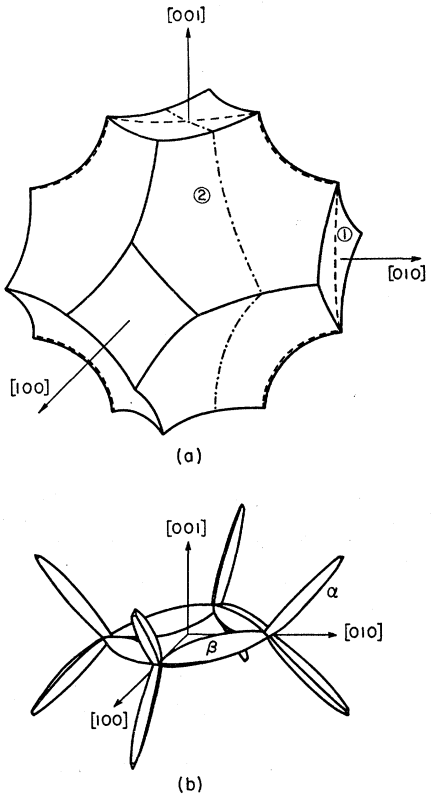

FIG. 12. (a) Free-electron second-zone Fermi surface for indium showing the effective zones for [100] and [1$\bar{1}$0] propagation. These are numbered 1 and 2, respectively. (b) Free-electron third-zone Fermi surface for indium showing the inequivalent α, β arms.

In two of the other four pure-mode (or nearly pure mode) directions, namely those normal to the (110) and (011) planes, the measured limiting slope values agree almost as well with the free-electron calculations. As noted previously, however, the agreement for propagation normal to (100) and (001) is poor, the measured limiting slopes being roughly half the free-electron values. Clearly in explaining these results we must consider the anisotropy of either the Fermi surface, the deformation parameter, or the mean free path, and perhaps even all three. Since for $a\gg1$, $d\alpha/df$ should be independent of l and since little is known about the deformation tensor, an investigation of possible Fermi surface effects seems to offer the best hope for understanding the disagreements just noted.

Indium is trivalent and has a face-centered tetragonal crystal structure. Its c/a ratio differs from unity by less than 8%, so that it has a Fermi surface very similar to aluminum. The important parts of the free-electron Fermi surface are the second-zone hole surface and the third-zone electron monster, both of which are shown in Fig. 12. Unlike aluminum, the third-zone arms α, β are not equivalent. The free-electron model also predicts

[30] P. N. Dheer, Proc. Roy. Soc. **A260**, 333 (1961).
[31] R. W. Morse, in *Progress in Cryogenics*, edited by K. Mendelssohn (Heywood and Company Ltd., London, 1959), Vol. 1, p. 242.

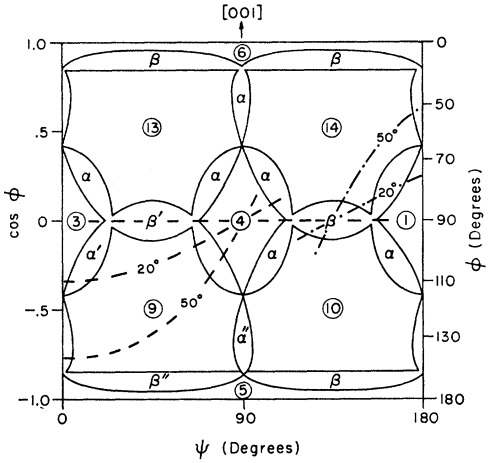

FIG. 13. Equal-area projection of one half of the free-electron Fermi surface for indium. Those sections of the sphere associated with the second-zone faces are numbered and those parts associated with the third zone are identified as part of an α or β arm. For propagation along [001], the effective zone is the line $\phi=90°$. The dashed and dot-dashed lines show the effective zones for propagation in the (010) plane at 20° and 50° toward [100] and in the (1$\bar{1}$0) plane at 20° and 50° toward [110], respectively

small pockets of carriers in the first and fourth zones, but these are removed by the lattice potential. Figure 12 also shows the effective regions ($\phi=\frac{1}{2}\pi$) on the second-zone surface in two of the major propagation directions for infinite ql. It is clear from this figure that, for propagation along [100], the effective region runs along the cusps of the second zone Fermi surface. Since $R=0$ for these cusps, it is obvious from Eq. (12) that they make no contribution to the attenuation. Thus the second zone only contributes approximately one half of the attenuation in the free-electron model, the remainder coming from the inside parts of the α arms. Similar considerations apply to the [001] propagation direction, the third-zone contribution arising in this case from the β arms. On the other hand, for propagation along [110], most of the contribution to the attenuation arises from the second-zone surface, since the effective region crosses surface edges but does not run parallel to any of them. For propagation along the normals to (011) and (111), an analogous situation occurs. Thus, there seems to be a correlation between the second-zone contribution and the ratio of measured attenuation to the free-electron value, i.e., the data seem to imply a near-zero contribution to the attenuation by the third-zone Fermi surface. Such an assumption also provides a qualitative explanation for the behavior of the (111) attenuation for intermediate ql. As ql is reduced, the β arms parallel to the plane $\phi=\frac{1}{2}\pi$ make up an increasing fraction of the widened effective zone. This can be seen quite clearly in the (111) projection of Fig. 14 to be described in Sec. IV B. If these arms make no contribution to the attenuation, then α/f will drop faster than the free-electron predic-

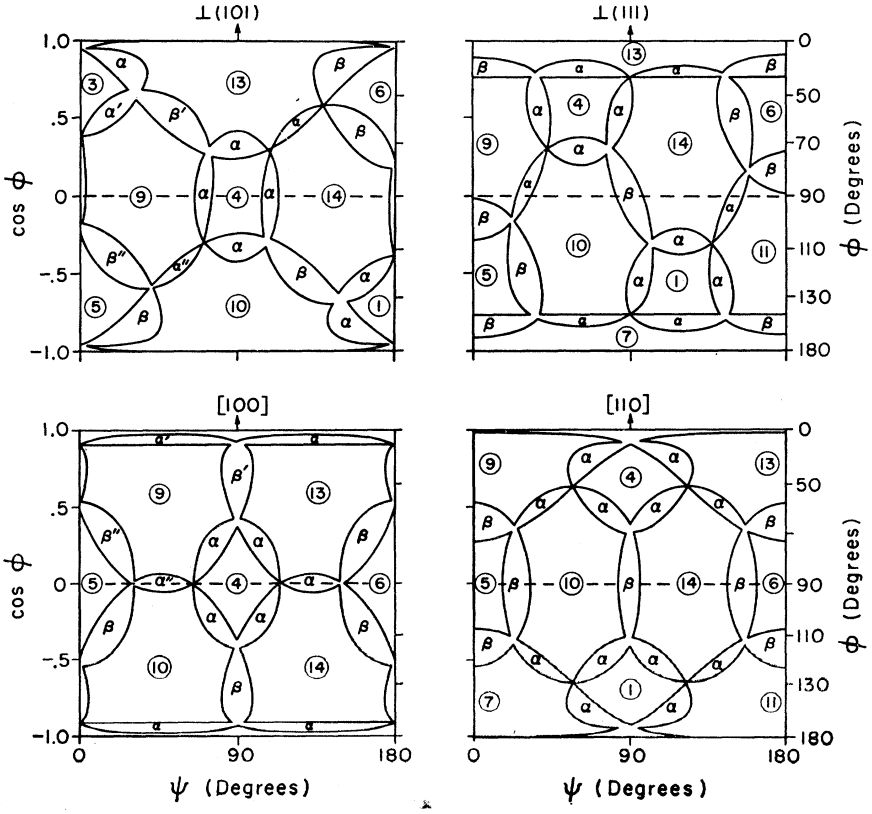

FIG. 14. Equal-area projections of one half of the free-electron Fermi surface for indium. The equatorial effective zones correspond to propagation along (101), (111), [100], and [001], respectively.

tion. Of course, the predicted high-frequency limiting value is also reduced somewhat because of the other third-zone arms. A possible reason for the high measured limiting value will be discussed later.

B. Quasilongitudinal Attenuation

To see if the same correlation is found for propagation directions between [001] and [100], we must subtract the contribution due to the J_2 term in Eq. (14) (the rapid-drop part of α_s) from the measured slopes of α versus f. The remainder may then be compared with the J_1 term, evaluated over the second-zone surface with the free-electron values of R and K_x. For all propagation directions in the (010) plane Ω can be shown to be less than 3 deg, using the known elastic constants of indium.[20] Thus, the second and third terms of Eq. (15) are negligible.

In order to see more clearly the location of the effective zone for various orientations, and at the same time to provide a means of graphically evaluating the J_1 term, it is convenient to show the effective zone path on some kind of projection of the Fermi surface. One type of projection is constructed as follows. The faces of the free-electron second-zone surface in Fig. 12 are segments of Fermi spheres centered on neighboring reciprocal-lattice sites. If each face is translated in reciprocal space by the vector required to bring the center of the associated sphere to the center of the Brillouin zone, then all of the second-zone faces are placed on the surface of a single sphere, and the face boundaries can be expressed in analytic form. Using spherical coordinates, an equal-area projection is constructed by plotting $\cos\phi$ versus ψ, where ψ is the azimuthal angle. If the coordinates are chosen so that $\phi=0$ is in the direction of propagation, then the effective zone will be along the equator ($\phi=\frac{1}{2}\pi$) of the projection. In Figs. 13 and 14 representative parts of the Fermi surface are plotted on equal-area projections for the five major propagation directions. On these projections, the relative contributions of the second and third zones can be determined by simply measuring their relative contributions to the effective zone length along the equator. Furthermore, for orientations other than these the effective zone can still be plotted, as shown in Fig. 13 for orientations 20° and 50° toward [100] and [110]. To measure the relative second- and third-zone contributions in such cases, the nonlinear character of the projection must be accounted for, but this presents no great problems. For propagation in the (010) plane, the results of such effective-zone calculations and data corrected for the rapid-drop part of α_s are given in Fig. 15. It is seen that the orientation dependence of the measured slopes $d\alpha/df$ is qualitatively the same as the variation of the second-zone Fermi surface contribution alone, except for the region within about 20° of the [100] direction.

At this point it is appropriate to consider what properties of the Fermi surface might explain the

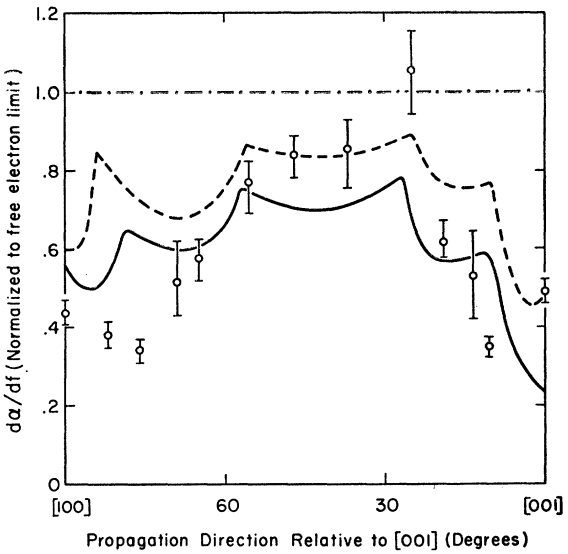

FIG. 15. Normalized limiting slopes $d\alpha/df$, minus the rapid-fall contribution, for quasilongitudinal waves propagating in the (010) plane of indium. The measured values are compared with the result obtained by subtracting the third-zone free-electron contribution for $ql\to\infty$ (dashed curve) and with a modification to account partly for the effects of the crystal potential on the second-zone surface for $ql=200$ (full curve).

apparent ineffectiveness of the third zone. Recent experimental data[3] and pseudopotential calculations[32,33] indicate that the crystal potential eliminates not only the first- and fourth-zone pockets, but also the third-zone α arms. This would certainly explain their ineffectiveness. If this is the case, however, then it is not sufficient to simply regard the α arms as making a zero contribution, while the second zone is unchanged. In the nearly-free-electron approximation[34] the disappearance of the α arms can be explained by the creation of energy gaps on the Brillouin zone boundaries, and if the lattice potential causes gaps at the $\mathbf{k}$ values corresponding to α arm locations, not only the α arms but also a part of the second zone will be affected. This is illustrated in Fig. 16, which shows a central cross section of the Fermi surface in the $(1\bar{1}0)$ plane. It is seen that the partial elimination of a third-zone β arm is accompanied by a rounding of the corresponding second-zone cusp. In the nearly-free-electron approximation the energy gap is centered at the energy given by $E=\hbar^2k_0^2/2m$, and this results in "removal" of equal parts of the arm and cusp. Thus it appears that when calculating the expected second band contribution to the effective zone, as much as twice the width of the α arms should be subtracted from the free-electron surface. The effect of subtracting this additional amount is seen in the solid curve of Fig. 15.

[32] N. W. Ashcroft and W. E. Lawrence, Phys. Rev. (to be published).

[33] W. J. O'Sullivan, J. E. Schirber, and J. R. Anderson (private communication).

[34] J. M. Ziman, *Principles of the Theory of Solids* (Cambridge University Press, London, 1964), p. 74.

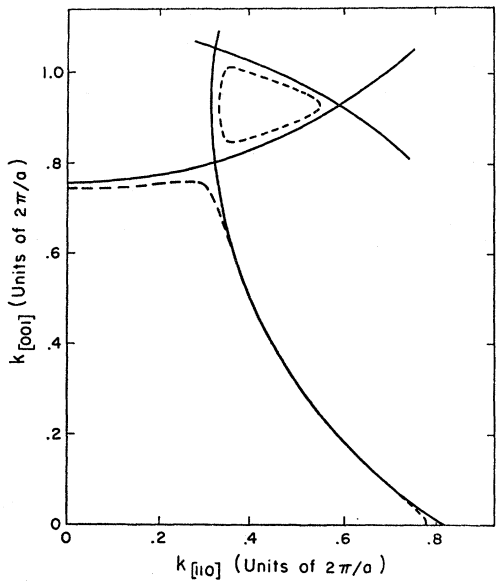

FIG. 16. Central cross section of the Fermi surface for indium in the (1$\bar{1}$0) plane. The full lines represent the free-electron surface and the dashed lines represent the results of a pseudopotential calculation (Ref. 33) with $V(11p)=-0.050$, $V(002p)=-0.031$, $V(200)=+0.007$ ry, where $p=a/c$.

The over-all agreement between the measurements and calculations is now somewhat better, the most obvious improvements being for propagation directions 0° to 30° from [100] and 5° to 20° from [001]. In the first region the sharp peak about 13° from [100] is partly smoothed out and the attenuation is reduced; a similar change occurs near [001]. The unexpectedly large difference between the two curves for propagation in the [001] direction is due partly to the additional amount of Fermi surface which has been subtracted and partly to the difference in calculation methods. The dashed curve, obtained by measuring effective zone lengths on the projections in Figs. 13 and 14, is based on the assumption of an infinite mean free path. In this case the effective zone has no width and the four α arms, which come very close to the equator of the [001] projection without crossing it, do not affect the attenuation. The solid curve results from numerical integration of the attenuation integral, given by the first term in Eq. (8), over the modified second zone for an assumed ql value of 200. This finite ql leads to an effective zone width on the order of 1°, so that the same four α arms do affect the calculated attenuation. Clearly the assumption of a finite ql is the more reasonable, and the dashed curve should be somewhat lower for [001] propagation. A similar explanation applies to the smaller difference between the two curves in the [100] orientation.

Fermi surface cross sections calculated from a recent set of pseudopotential parameters[33] suggest that the assumption of equal effects on the third-zone α arms and the associated second-zone cusps is reasonable except near the ends of the arms. In Fig. 17 the dot-dash curve shows the effect of subtracting half the width of the associated α arm from the second-zone [011] free-electron cusp. It is seen that the pseudopotential calculations given by the dashed curve predict a larger deviation near the ends of the third-zone arms, in such a way as to round off the corners of the second zone surface quite severely. By noting the way in which the effective zone changes with orientation on the projections of Figs. 13 and 14, it can be seen that the contribution of these second-zone corners to the attenuation is directly related to the presence of sharp peaks in the calculated attenuation curves of Fig. 15. Thus removing these corners, a crude approximation to the rounding which actually takes place, would be expected to further improve the agreement between experiment and theory in Fig. 15, particularly for orientations 5° to 20° from [100].

The apparent ineffectiveness of the third-zone β arms can be at least partly explained by considering the effect of the crystal potential in rounding off the edges of the arms and associated second zone cusps. Rounding these edges has two effects: it reduces the length of any effective zone crossing the edge, and, at the same time, changes the Gaussian curvature at points on and near the edges, as can be seen in Fig. 16. Since the reduction of the effective zone length is negligible for effective zones which run along an arm and never cross the edges, the importance of the first effect depends strongly on orientation. The attenuation change due to the second effect is also orientation-dependent, because the dependence of Eq. (12) on the Gaussian curvature does not necessarily mean that a region of high curvature makes a small contribution to the attenuation. Equation (12) can be rewritten as

$$\alpha_{a\gg 1}=\frac{\hbar q}{4\pi^2 M v_s}\oint R_\phi(\phi=90°,\psi)R_\psi(\phi=90°,\psi)K_x^2 d\psi$$

$$=\frac{\hbar q}{4\pi^2 M v_s}\oint R_\phi K_x^2 dL_\psi, \tag{19}$$

where dL_ψ is the differential length measured along the effective zone and R_ϕ is the radius of curvature in the plane defined by $\psi=$ const. The angles ϕ and ψ are labelled in Fig. 18. When the equation is written this way, it is clear that only the radius R_ϕ can affect the attenuation. This is reasonable since it is R_ϕ that determines the width of the effective zone.

To estimate the magnitude of these effects in indium, it is necessary to know something about the actual dimensions of the β arms. de Haas–van Alphen measurements[35] indicate that the normal cross-sectional area of the β arms is approximately half of the free-electron prediction. It can be shown that any two-dimensional geometric figure (such as the β-arm cross section), whose

[35] G. B. Brandt and J. A. Rayne, Phys. Rev. 132, 1512 (1963).

area is halved while its shape is held constant, will have a final perimeter equal to $1/\sqrt{2}$ times the original perimeter. Any increase in the ratio of area to perimeter during the area change, such as will occur from the rounding of sharp corners, will result in a further decrease of the perimeter. Thus, it may be estimated that the effective zone around a β arm has approximately 60% of its free-electron length. If the crystal potential has a similar effect on the corresponding second-zone cusp, then the length of an effective zone crossing a β arm at right angles may be shorter than the free-electron value by up to 80% of the free-electron β-arm width. When the effective zone crosses at an angle less than 90°, as for propagation directions 0° to about 35° from [100], the effect will be somewhat less. However, a significant reduction in R_ϕ also occurs near the arm and cusp edges for these orientations, so that the total drop in attenuation associated with the β arms may be roughly equal to the drop calculated by assuming the β arms to be totally ineffective.

For propagation in the [001] direction the effective zone runs lengthwise along the β arms, as seen in Fig. 13. Therefore, the reduction in its length is small, perhaps 15%, and R_ϕ is significantly decreased over only about one quarter of this length. Although both the effective-zone length and R_ϕ are also less than the free-electron value near the corners of the second zone [100] faces, it seems clear that for this orientation a reduction of the attenuation by an amount equal to the total β arm contribution is too large a correction to the free-electron value. A more reasonable estimate, based on the above corrections to the β arms and similar ones for the [100] faces, raises the solid curve of Fig. 15 to approximately 0.54, much nearer the measured value. This includes a contribution of about 2% from the rounded cusps of the β arms and the second zone. For orientations a few degrees away from [001], the model becomes more

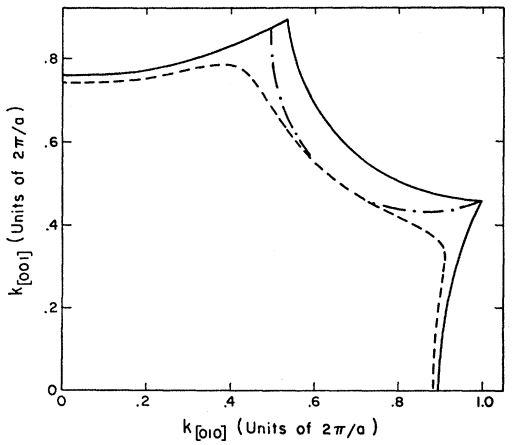

FIG. 17. Central cross section of the second-zone Fermi surface for indium in the (100) plane. The free-electron and pseudopotential predictions are given by the full and dashed curves, respectively, while the dot-dashed curve shows the effect of the modification discussed in the text.

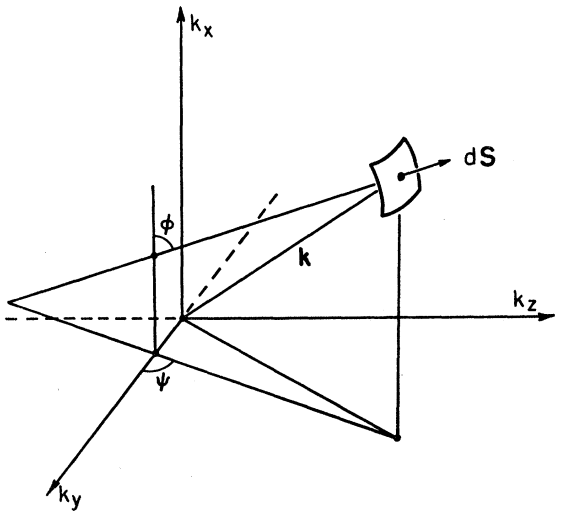

FIG. 18. Coordinate system for sound propagation in the x direction.

reasonable again since the effective zone nears the edge of the β arm and the adjoining second-zone face, where R_ϕ is reduced to a few percent of its free-electron value. In fact, the low value of R_ϕ near the edge of the second zone will cause the area of reduced attenuation to extend several degrees past the sharp rise exhibited by the curves in Fig. 15, bringing them more nearly in agreement with the data.

The one feature of the experimental results which remains unexplained by the preceding discussion is the high attenuation 25° from the [001] direction. Clearly an attenuation greater than the free-electron value cannot be explained by assuming the absence or ineffectiveness of some part of the Fermi surface. A flat area near the central part of the (111)-type faces, leading to a high value of R_ϕ along part of the effective zone, could explain the increased attenuation. However, recent size-effect measurements[36] put an upper limit of about 10% on the deviation from free-electron curvature near (111). The only remaining adjustable parameter is the deformation coefficient. Thus it appears that K_x must exceed the free-electron value on the (111)-type faces in the region crossed by the effective zone for propagation approximately 25° from [001]. This region is also crossed by the effective zones for propagation normal to (111) and (110), but this leads to no conflict. On the contrary, it may explain why the predicted attenuation for these orientations, after subtracting the contribution of the third-zone arms, is less than the measured value as indicated in Table I.

C. Rapid-Fall Attenuation

The lower curve in Fig. 7 is drawn through the measured values of rapid-fall attenuation, as described

[36] I. P. Krylov and V. F. Gantmakher, Zh. Eksperim. i Teor. Fiz. **51**, 740 (1966) [English transl.: Soviet Phys.—JETP 24, 492 (1967)].

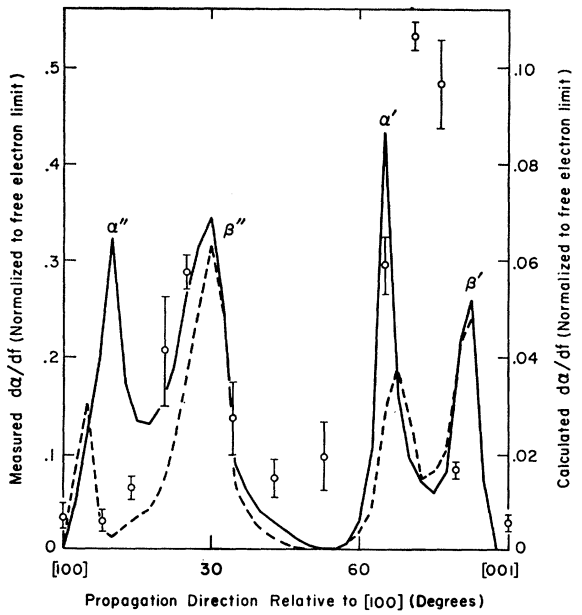

FIG. 19. Normalized contribution to the limiting $d\alpha/df$ arising from the rapid-fall region for quasilongitudinal waves propagating in the (010) plane of indium. The dashed curve shows the calculated variation obtained by subtracting the third-zone contribution in the limit $ql \to \infty$, while the full curve shows the variation obtained with the modified second-zone surface for $ql = 200$.

previously. This part of the total attenuation is associated with the J_2 term in Eq. (14), where J_2 has the theoretical form given by Eq. (16). From the symmetry properties for propagation in the (010) plane, L_1, L_2, and L_3 are found to be

$$L_1 = A^2/\pi A_{yy}, \quad L_2 = 2AB/\pi A_{yy}, \quad L_3 = B^2/\pi A_{yy}, \quad (20)$$

where

$$A = \int_S (K_x + k_x \cos\phi) \tan\phi \cos\psi dS,$$
$$B = \int_S (K_y + k_y \cos\phi) \tan\phi \cos\psi dS, \quad (21)$$

and the integrals A_{ij} have the form given in Eq. (9). For a pure longitudinal mode Ω is zero, causing the L_2 and L_3 terms in Eq. (16) to vanish. Since pure modes propagate only in high-symmetry directions, and since $k_x = k_0 \cos\phi$, the change in sign of $\tan\phi$ at $\phi = \frac{1}{2}\pi$ causes both parts of A, and thus L_1, to vanish also.

For quasilongitudinal modes, which propagate in directions of lower symmetry, A will have a nonzero value when the Fermi surface has asymmetry on opposite sides of $\phi = \frac{1}{2}\pi$. In fact, for a model in which pieces of the surface are assumed to be absent or ineffective, it may become quite large for some propagation directions. The same arguments apply for that part of B containing K_y. However, k_y contains a factor $\sin\phi$ which gives an even integrand when combined with $\cos\phi$ and $\tan\phi$. Thus, the second part of B always has a value on the order of (k_0^3). This is the same order of magnitude as values calculated for A in the (010) plane, but L_2 and L_3 can still be neglected for approximate evaluation of Eq. (16), since Ω is always less than 3° in this plane.

The integral $J_2 \cong L_1$ has been evaluated by numerical integration of A and A_{yy} over the model Fermi surface obtained by assuming the third zone to be ineffective, and also for the model which removes an additional amount equal to the width of the associated α arm from each second-zone cusp. The results are shown in Fig. 19 along with the experimental data plotted on a reduced scale. It is believed that the nonzero values measured for [001] and [100] propagation probably reflect systematic errors in the extrapolation procedure used to reduce the data. The calculated curves exhibit two pairs of peaks, each pair occurring in the same range of propagation directions as one of the two peaks in the data. Furthermore, the appearance of double peaks in the calculated curves and the discrepancy in the calculated and measured magnitudes can be explained in qualitative terms by the known inaccuracies of the model. Since the model for the dashed curves makes no correction for the effect of the crystal potential on the second-zone surface near the α arms, the discussion may be limited to the solid curve.

The structure in the calculated curve is due almost entirely to the numerator of L_1 in Eq. (20), i.e., the integral A. Since this integral is zero when evaluated over the entire Fermi sphere, it can be computed for the modified surface by evaluating Eq. (21) over each of the third-zone arms (with the α arms assumed to have double their free-electron width), and adding the results. The sum obtained is equal, with a change in sign, to the integral A for the modified second zone. Although all of the third-zone arms contribute to the integral, four of the arms (in each quadrant of the surface) dominate. These arms are indicated by single and double prime markings in the left quadrant of the [001], (101), and [100] projections in Figs. 13 and 14; the associated peaks are labelled in Fig. 19. The separation of these peaks is caused by the nearly zero width of the arms at the points where they join and, in the case of β', by the assumption of total ineffectiveness of the β arm instead of ineffectiveness at the edges of both the β arm and the corresponding second-zone cusp. Thus, it can be seen that the rounding of the second-zone corners and cusps on the actual Fermi surface would tend to eliminate the separate identity of the α and β arms in the evaluation of A and would give two single peaks between the [001] and [100] orientations. This tendency would be further enhanced by the wider peaks resulting from a more gradual transition between effective and ineffective areas, as expected for the actual Fermi surface.

These arguments also provide a possible explanation for the magnitude discrepancy. Since the integral is

squared in the expression for L_1, the effect of combining two peaks in A is to give a single peak with a height greater than the combined heights in Fig. 19. The calculated curve might then reach the measured peak values, which are larger than the present calculations by a factor of 4 or more. Although it is not clear how the relative magnitudes of the single and double prime peaks in Fig. 19 are affected by the preceding discussion, it can be seen from the positive sign of the k_y part of the integral B that the L_2 terms in Eq. (16) may be expected to enhance the peak near [001] and reduce that near [100]. As previously noted, the importance of this effect is limited by the small value of Ω.

D. Edge Effects

It has been proposed that there are reasons, essentially independent of the crystal-potential effects on the Fermi surface, for expecting the electrons near the sharp edges of the free-electron Fermi surface to be ineffective in attenuation.[9] In addition to having some doubts about the validity of the arguments presented, the present authors believe the predicted effects to be negligible for a real Fermi surface, i.e., one whose edges are rounded by the crystal potential.

V. CONCLUSIONS

Low-temperature measurements of the electronic part of the acoustic attenuation in single-crystal indium have been reported for a wide range of strain amplitude, frequency, orientation, and purity in both the superconducting and normal states. It has been shown that the attenuation exhibits significant amplitude dependence except at very low strain amplitudes. This amplitude dependence is found to agree qualitatively with the predictions of a dislocation damping mechanism, but satisfactory quantitative agreement with present theories is not obtained. The effects of amplitude dependence can be largely eliminated by extrapolating to zero amplitude, and theoretical arguments suggest that the error due to dislocations at zero amplitude is small.

The measured electronic attenuation values have the expected quadratic and linear frequency dependence in the low- and high-frequency limits, respectively. However, the high-frequency limiting slopes and the intermediate ql frequency dependence have been observed to exhibit considerable deviation from the predictions of the free-electron model. The limiting slope values of α_n versus f are highly anisotropic and for quasi-longitudinal waves include a significant contribution which vanishes in the superconducting state within approximately 30 mdeg below T_c. This drop is in addition to the less sudden drop of the usual BCS attenuation for longitudinal waves.

The deviations from free-electron behavior, including the observation of a large rapid-fall attenuation at T_c, have been largely attributed to those features of the Fermi surface topology arising from effects of the crystal potential. The apparent absence of the α arms is the most notable of these, but other relatively minor modifications to the free-electron surface, such as the rounding of corners and cusps, have been shown to be important in determining attenuation values. These conclusions are supported by a comparison of the experimental results with calculations intended to incorporate the basic effects of the crystal potential. Although Fermi surface topology has been proposed as the dominating factor, it is also noted that some anisotropic departure from the free-electron value of K_x is likely.

There are a number of interesting possibilities for continued investigation of the electronic attenuation in indium. It is clear that attenuation calculations based on a complete and accurate pseudopotential model for the second- and third- zone Fermi surfaces are needed at this time. Such calculations can be expected to establish more conclusively the degree to which Fermi surface topology can account for the deviations from free-electron behavior. They should also make it possible to extract more information about the deformation parameter.

If more accurate calculations prove to be successful in predicting the present limiting-slope values (including the rapid-fall contribution), two additional steps might be taken. First, it is of interest to see what sort of anisotropy may exist for propagation in the (001) and (110) planes. If any striking features are predicted, additional measurements might be undertaken as a further check of the model. Second, once a reasonable degree of confidence is gained in some model of the Fermi surface topology, and noticeable progress has been made in determining the anisotropy of the deformation parameter, further studies of the ql dependence of attenuation may be useful for investigating the possibility of anisotropy in l.

Finally, it should be noted that nothing has been found which can be said to conflict with the presently available theories for electronic attenuation. This is not the case for the theories of dislocation attenuation, however, and further progress in this area is to be desired.

ACKNOWLEDGMENTS

Thanks are due to K. C. Hepfer, who obtained the residual resistance ratios for the samples used in these experiments. The authors are also grateful to Dr. J. R. Anderson and Dr. N. W. Ashcroft for supplying the results of their pseudopotential calculations for indium prior to publication. Helpful discussions with Dr. J. R. Leibowitz and Dr. A. C. E. Sinclair are also acknowledged. This work was supported by a grant from the National Science Foundation.